Article

Not peer-reviewed version

Influence of Al and Ti Alloying and Annealing on the Microstructure and Compressive Properties of Cr-Fe-Ni Medium-Entropy Alloy

Keyan An , Tailin Yang , Junjie Feng , Honglian Deng , Xiang Zhang , Zeyu Zhao , Qingkun Meng , Jiqiu Qi , FuXiang Wei * , Yanwei Sui *

Posted Date: 24 September 2024

doi: 10.20944/preprints202409.1787.v1

Keywords: high-entropy alloy; Al and Ti elements; annealing heat treatment; second phase strengthening; compressive properties

Article

Influence of Al and Ti Alloying and Annealing on the Microstructure and Compressive Properties of Cr-Fe-Ni Medium-Entropy Alloy

Keyan An [1,2], Tailin Yang [1], Junjie Feng [1], Honglian Deng [1], Xiang Zhang [1], Zeyu Zhao [1], Qingkun Meng [1], Jiqiu Qi [1], Fuxiang Wei [1,*] and Yanwei Sui [1,*]

[1] Jiangsu Province Engineering Laboratory of High Efficient Energy Storage Technology and Equipments, School of Materials and Physics, China University of Mining and Technology, Xuzhou, 221116, China
[2] Huaihai Holding Group, Xuzhou, 221116, China
* Correspondence: weifuxiang2001@163.com; suiyanwei@cumt.edu.cn

Abstract: This research investigates the impact of Al and Ti elements on the formation of self-generated ordered phase in high-entropy alloys (HEA), which have been receiving widespread concentration in present times thanks to their remarkable multifunctional properties and wide range of component selection. By adjusting the dual elements of Al and Ti, the study explores the regulation of quantity and distribution of the in-situ self-generated ordered phases in the alloy. The results of the annealing heat treatment process demonstrated that, through accession Al and Ti elements, the Cr-Fe-Ni medium-entropy alloy transfer from BCC phase to BCC+FCC phase and the precipitation of new phases such as B2, L21, and σ. This led to a synergistic impact of second phase strengthening, and also of solid solution strengthening, resulting in improved compressive properties of HEA.

Keywords: high-entropy alloy; Al and Ti elements; annealing heat treatment; second phase strengthening; compressive properties

1. Introduction

HEA have garnered extensive notice since their inception, which is due to their exceptional comprehensive properties and versatile design space [1–3]. Numerous studies have confirmed that, as a novel alloy system, high-entropy alloys can be synthesized, processed, and analyzed, with great potential for applications in various domains such as soft magnetic materials, structural materials, hydrogen storage materials, electrothermal alloy materials, and anti-corrosion materials [4–8].

In an effort to seek high-entropy alloy with prime multifunctional properties, various strengthening methods have been continuously attempted. Alloying is the oldest and most effective method of strengthening methods, the selection of elements is the key to the effectiveness of alloying. At present, the alloying of high entropy alloys mostly focuses on adding a new element or simply regulating a single element. For example, Yuan et al. [9] enhanced the mechanical properties of a FeMnCoCr-based HEA by Cu alloying, the alloy doped with 0.3% Cu achieved a yield strength of 768 MPa, tensile strength of 960 MPa and uniform elongation of 33.6%. Zhang et al. [10] improved the corrosion resistance of CoCrFeMnNi HEA by Nb alloying. Liu et al. [10] discovered that, for Si micro-alloyed alloys, the annealed $(Ti_{28}Zr_{40}Al_{20}Nb_{12})_{100-x}Si_x$ (x=0, 0.1, 0.2, 0.5) HEA shown an increase of compression strength and fracture strain.

Literatures have shown that CrFeNi is a well-studied, FCC-structured medium-entropy alloy with a relatively simple phase composition [10–13]. To take advantage of the atomic hysteresis diffusion effect in high-entropy alloys, elements with a large difference in atomic radius and strong bonding with alloy components are added to generate in-situ, particle-reinforced phases in high-entropy alloys [14–17]. This is achieved through rapid solidification in water-cooled arc-melted

 doi:10.20944/preprints202409.1787.v

copper disks, which exploits the unique characteristics of this method of fabrication [18–20]. It is difficult to control the size, morphology, and volume fraction of nano ordered precipitate phase in CrFeNi alloy solely by adjusting the proportion of Al element. Ti element, which is similar to Al element and has a larger size, and a lower enthalpy of mixing with post transition metal elements [21]. The dual element alloying of Al and Ti elements can induce second phase precipitation, and combined with heat treatment technology, it is expected to achieve precise regulation of precipitation phases in the alloy.

This study introduces Al and Ti elements with large atomic radius and propensity for easy precipitation into the CrFeNi high-entropy alloy to generate in-situ particle-reinforced particle phase, thereby enhancing the compressive properties of HEA. The research focuses on the AlCrFeNiTi alloy, and the microstructure and compressive properties of the alloy are evaluated in different situations.

2. Experimental Methods

The purity and proportion of the five metallic elements, must be carefully determined to obtain the desired final phases. Theoretical phase formation standards available in documents were used to estimate the final phases of each alloy [22–24].

(1) To minimize the presence of impurities and other elements, the selected raw materials are high-purity metals with a purity of more than 99.9%. To account for the volatility of Al during the smelting process, additional 1% of Al is added to the batch to compensate for any losses.
(2) The proportioning of the metal elements is baseed on the molar ratio, with the molar content of Al and Ti in the alloy adjusted while maintaining the constant ratio of Cr-Fe-Ni. Alx(CrFeNi)88Ti(12-x)(x=9,8,6,4,3) is abbreviated as A9T3, A8T4, A6T6, A4T8, and A3T9 in the following context. This study investigates the influence law of Al and Ti dual element alloying on the microstructure and compressive properties of the Cr-Fe-Ni medium-entropy alloy.
(3) This study examines the impact of intermediate temperature annealing on the microstructure and compressive properties of the Cr-Fe-Ni medium-entropy alloy, and attempting to clarify the strengthening and deformation mechanisms of alloy.
(4) The following four tables (Tables 1–4) list the relevant parameters of each element in high entropy alloys.

Table 1. Basic properties of alloying elements.

element	Al	Cr	Fe	Ni
atomic weight, g/mol	26.98	52	55.85	58.69
atomic radius	1.432	1.249	1.241	1.246
melting point, °C	660.25	1857	1535	1453
Crystal Structure (Low Temperature)	FCC	BCC	BCC	FCC
Crystal Structure (High Temperature)	FCC	BCC	BCC	FCC

Table 2. Mass percentage and theoretical melting point of AlxCrFeNiTiy alloy components.

alloy	Al/wt. %	Cr/wt. %	Ti/wt. %	Fe/wt. %	Ni/wt. %	Theoretical melting point
$Al_9(CrFeNi)_{88}Ti_3$	5	29	3	31	33	1795.21 K
$Al_8(CrFeNi)_{88}Ti_4$	4	29	4	31	33	1802.48 K
$Al_6(CrFeNi)_{88}Ti_6$	3	29	5	31	32	1817.02 K
$Al_4(CrFeNi)_{88}Ti_8$	2	28.37	7.12	30.46	32	1831.56 K
$Al_3(CrFeNi)_{88}Ti_9$	1.499	28.26	7.988	30.351	31.90	1838.83 K

 doi:10.20944/preprints202409.1787.v

Table 3. Thermodynamic data of AlxCrFeNiTiy alloy.

alloy	$\triangle H_{mix}$	$\triangle S_{mix}$	δ/%	VEC	Ω	T*m*/k
$Al_9(CrFeNi)_{88}Ti_3$	-10.383	11.649	4.7	7.43	1.6	1795.21 K
$Al_8(CrFeNi)_{88}Ti_4$	-10.631	11.723	4.7	7.44	1.635	1802.48 K
$Al_6(CrFeNi)_{88}Ti_6$	-11.055	11.78	4.8	7.46	1.705	1817.02 K
$Al_4(CrFeNi)_{88}Ti_8$	-11.382	11.723	4.9	7.48	1.778	1831.56 K
$Al_3(CrFeNi)_{88}Ti_9$	-11.51	11.649	4.9	7.49	1.817	1838.83 K

Table 4. Mixing enthalpy between elements.

Mixing enthalpy	Ti	Cr	Al	Fe	Ni
Ti	0	-7	-30	-17	-35
Cr		0	-10	-1	-7
Al			0	-11	-22
Fe				0	-2
Ni					0

2.1. Alloy Sample Preparation Method

The Alx(CrFeNi)88Ti(12-x) alloys were fabricated using non-consumable vacuum are melting and non-consumable vacuum induction melting technologies, respectively [25]. With the aim of reducing material waste, increasing chemical homogeneity, and minimizing pollution. By regulating the elements Al and Ni, this study seekd to control the content of NiAl intermetallic compound phase and Ni_3Al intermetallic compound phase in the alloy, as well as the self-generated NiAl nanophase in the alloy [26,27].

2.2. Homogenization Annealing

The change in the properties of the alloy and factors influencing it are analyzed by comparing the characterization and test results of the as-cast alloy. Certain as-cast alloy samples were subjected to homogenization annealing the use of the Hefei Kejing KSL 1400 A3 box furnace. The annealing process involved heating the samples to 800 °C at a rate of 5 °C/min, keeping warm for 8 hours, then slowly cooling the samples in the furnace.

2.3. X-ray Diffraction Analysis

The smelted alloy ingot was transformed into a 15 mm × 15 mm × 3 mm cube sample using wire electric discharge cutting technology. The cut sample was subjected to multiple rounds of polishing with 180-2000 # SiC sandpaper, starting with coarse sandpaper and progressing to finer sandpaper to remove the wire cutting marks on the surface. The sample was then ultrasonic cleaned in pure ethanol to remove any remaining impurities and oil stains on the surface [28].

2.4. Scanning Electron Microscopy Analysis

In this study, the SEM samples were smoothed by 180-2000# Sic sandpaper and subjected to mechanical polishing and aqua regia corrosion treatment under specific conditions [29].

2.5. Transmission Electron Microscopy Observation

Detailed observation of the microstructure of the alloy using high-resolution field emission transmission electron microscopy (FEI Tecnai G2 F20, TEM), and characterize the crystal structure by

 doi:10.20944/preprints202409.1787.v

using selected area electron diffraction (SAED) [30,31]. Requirements for the test sample: cut the alloy sample into 10 × 10 × 1 (mm) thin sheet using wire electric discharge cutting technology, then stick the sample onto a smooth and flat surface of the metal block, grind sheet to a thickness of approximately 0.4 mm with a pre grinder, then use ion thinning to reduce the thickness of the sheet to 100 μm below, punch it into a circle with a diameter of 3mm, further thinning the sample to perforation using electrolytic double spray method [32].

2.6. Compression Performance Evaluation of Alloy at Room Temperature

The alloy samples were cut into cylinders shapes with a height of 10 mm and a diameter of 5 mm using wire electric discharge cutting technology, on the basis of the standard "Test Method for Compressive Properties at Room Temperature" (GB T7314-2005). To minimize the impact of wire cutting marks on the subsequent compression performance testing, the wire speed of the molybdenum wire in the wire cutting machine was reduced to the lowest possible level. The samples were then smoothed with 1500# SiC sandpaper to remove any burrs on the surface, and ultrasonically cleaned in pure ethanol [29].

The compression performanceat room temperature was tested using a Shimadzu AG-XPLUS vertical 100 kN electronic universal testing machine. The testing process recorded the loading force and stroke data, which was then used to plot the quasi-static compression engineering stress-strain curve using Origin data processing software. This allowed for a detailed analysis and comparison of the sample's strength, plasticity, and other mechanical properties [33,34].

3. Results and Discussions

3.1. Analysis of Phase and Surface Morphology

Figure 1a illustrates the XRD patterns of as-cast alloy, Figure 1b illustrates the XRD patterns of annealed alloy. As shown in the Figure 1a, the addition of Al and Ti caused the appearance of BCC phase diffraction peaks and the precipitation of ordered phases B2 and L21. The presence of σ phase was observed when the Al and Ti content was A8T4 and A4T8, indicating that the dual-element alloying of Al and Ti caused the crystal structure change from FCC phase to FCC+BCC phase, resulted in a significant increase in precipitated phase. After annealing at 800 °C, besides the aforementioned transformation, the L12 phase was also separated out. The Ni3Al intermetallic phase was formed when the Al and Ti content was A8T4 and A4T8. The diffraction peaks of each crystal plane demonstrated good agreement, suggesting that the long-time annealing treatment provided sufficient energy for the proliferation of alloying elements and relieved lattice distortion.

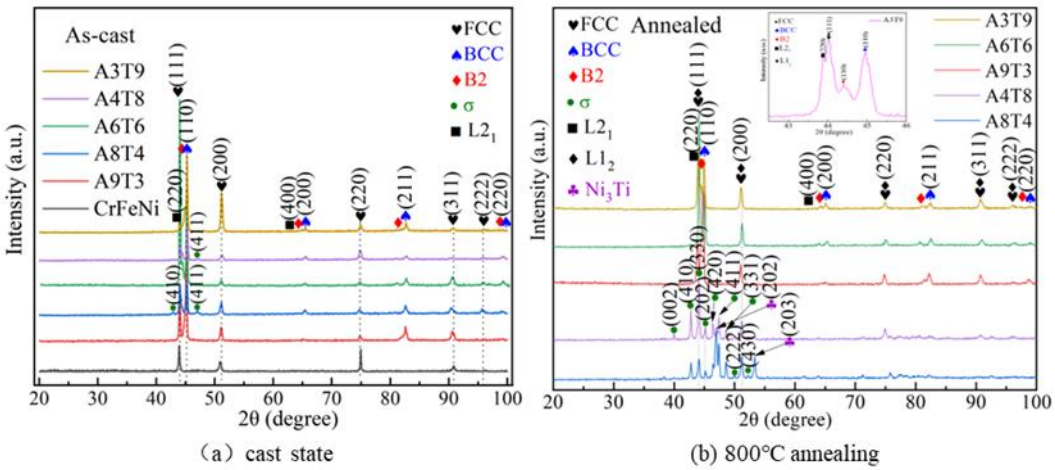

Figure 1. XRD patterns of as-cast and annealed alloys: (a) at cast; (b) after annealing.

Figure 2 exhibits the OM images of cast samples with various compositions. It can be noticed that the cast samples presents a classic dendrite structure, as depicted in Figure 2a–d. The dendrite

 doi:10.20944/preprints202409.1787.v

structure becomes finer with increasing Ti content. Figure 3 exhibits the OM images of alloy samples with different compositions after annealing at 800 °C. In comparison to the as-cast alloy, the dendrite structure of A9T3, A6T6, and A3T9 remains after annealing. However, a considerable number of black, bar-like phases are evident within the light-colored phase, indicating the formation of a new phase because of the annealing heat treatment.

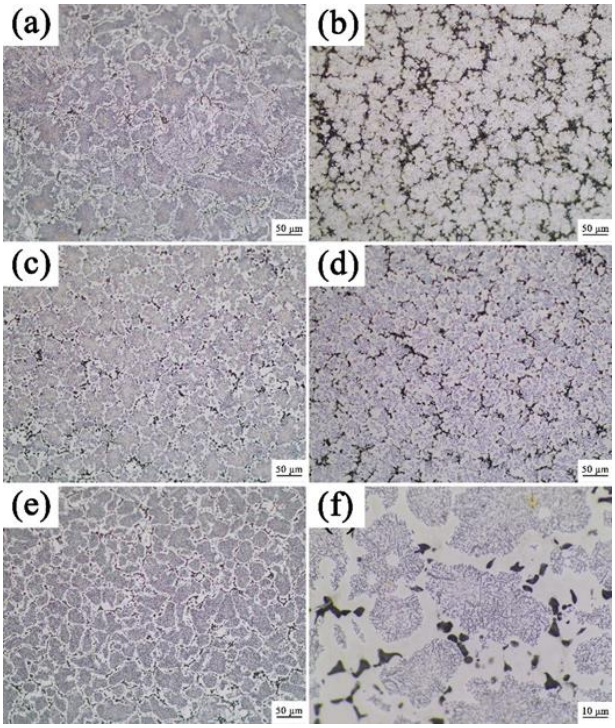

Figure 2. The OM images of as-cast: (a) A9T3; (b) A8T4; (c) A6T6; (d) A4T8; (e) A3T9; (f) A6T6.

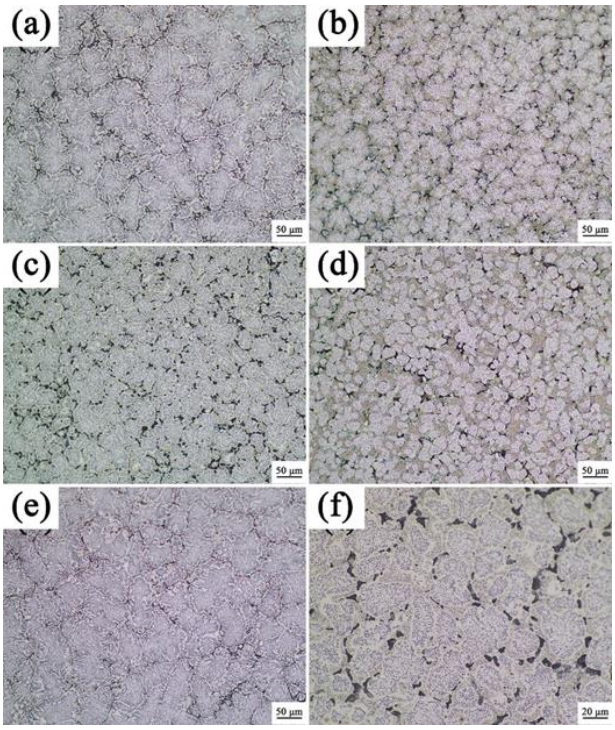

Figure 3. The OM images of the alloy after annealing at 800°C: (a) A9T3; (b) A8T4; (c) A6T6; (d) A4T8; (e) A3T9; (f) A6T6.

 doi:10.20944/preprints202409.1787.v

Figure 4 displays the SEM-BSE image of the cast alloy after exposure to corrosion. All alloy compositions exhibit a dendrite structure, labeled as A phase (interdendritic structure) and B phase (dendritic structure). The black elongated phase, referred to as C phase, is a precipitated phase found between the dendrites and is primarily located within the A phase. The average size of the dendrite structure in each composition was calculated using ImageJ software, with the average dendrite sizes in A9T3, A8T4, A6T6, A4T8, and A3T9 alloys being 78, 28, 52, 24, and 74 μm, respectively. The A4T8 alloy had the smallest dendritic structure, while the dendrite structure in the A3T9 alloy appeared abnormally coarse when the T content reached 9%. Figure 5 presents a surface scan diagram of the element distribution in the as-cast alloy, indicating that the A phase has a large content of Ni and Fe elements, the B phase has a large content of Cr and Fe elements, and the C phase has a large content of Al, Ti, and Ni elements. Failure to observe obvious differences in the distribution of Fe element between the A and B phases.

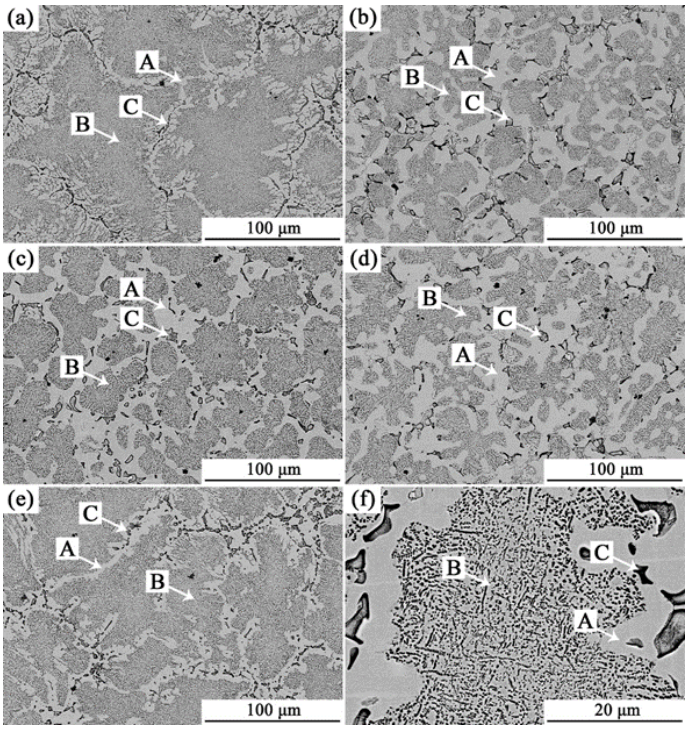

Figure 4. SEM-BSE image of the as-cast alloy: (a) A9T3; (b) A8T4; (c) A6T6; (d) A4T8; (e) A3T9; (f) A6T6.

 doi:10.20944/preprints202409.1787.v

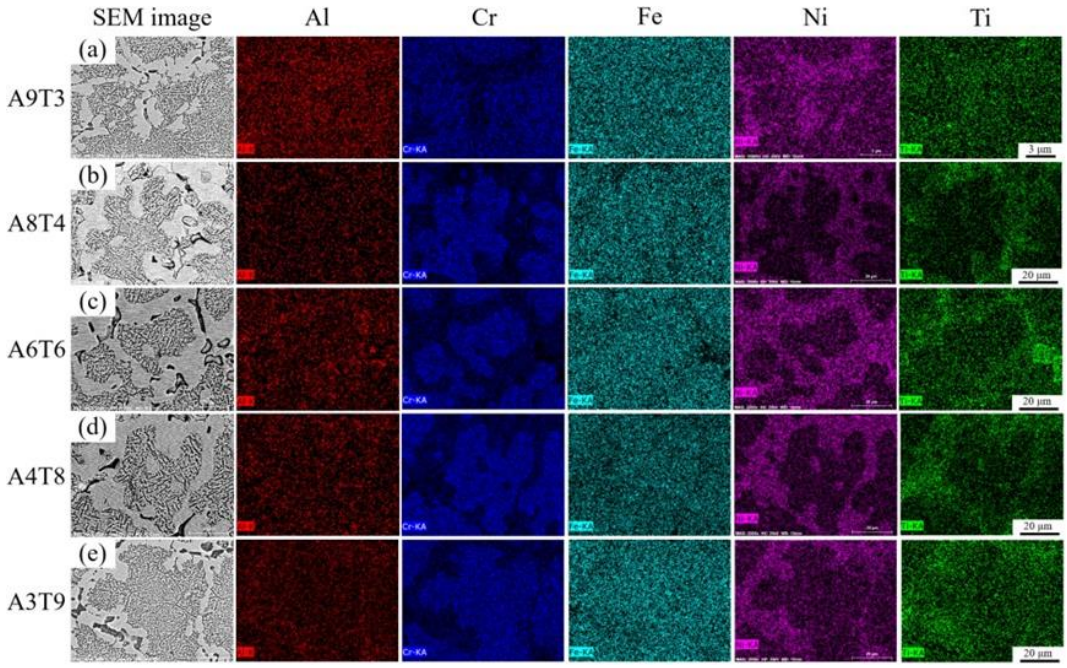

Figure 5. Surface scan of as-cast alloy: (a) A9T3; (b) A8T4; (c) A6T6; (d) A4T8; (e) A3T9.

Figure 6 exhibits the SEM-BSE image of the alloy after undergoing annealing and corrosion treatment. The phase composition rules are the same for A9T3, A6T6, and A3T9 alloys. The microstructure of the annealed samples do not undergo significant changes compared to the two-phase interwoven network structure in the as-cast state, with only new phases precipitated from the dendrite and interdendritic regions. Same as Figure 4, labeled as A phase (interdendritic structure) and B phase (dendritic structure). The black elongated phase, referred to as C phase, is a precipitated phase found between the dendrites and is primarily located within the A phase. Figure 6f is a locally enlarged view of Figure 6c, C phase is mainly distributed in A phase. Round rod shaped light colored phase was observed in the B phase, which is consistent with the color of A phase. Compared to as-cast alloys, the previously nanoscale particles in B phase exhibit growth phenomenon, the size has increased from a few hundred nanometers to a few micrometers. The microstructure and morphology changes in A8T4 and A4T8 alloys demonstrate the same regularity exhibit a similar pattern, becoming disordered while still retaining the dendrite structure observed in the as-cast state. To gain further insight into the composition distribution of the alloy after annealing heat treatment, a mapping scan was conducted, and the outcome are displayed in Figure 7. The microstructure morphology of A9T3, A6T6, and A3T9 alloys are distinct from those of A8T4 and A4T8 alloys and are discussed in this section. In A9T3, A6T6, and A3T9 alloys, the elements Al, Ti, Cr, Fe, and Ni segregate on the basis of the following patterns: the interdendritic structure has a large content of Fe, Ni elements, the dendrite structure has a large content of Cr, Fe elements, and the black long strip phase within the interdendritic structure has a large content of Al, Ti and Ni elements. Additionally, there is a white granular phase within the black strip phase, which has a large content of Cr, Fe elements. In A8T4 and A4T8 alloys, there are also variations in the distribution of each element: the interdendritic structure has a large content of Ni, Fe and Cr elements, the dendrite structure has a large content of Cr, Fe elements, the lamellar structure has a large content of Ni, Ti elements, the black striped region (C phase) has a large content of Al, Ni, and Ti elements, and the granular phase within the interdendritic structure has a large content of Al, Ni, and Ti elements.

 doi:10.20944/preprints202409.1787.v

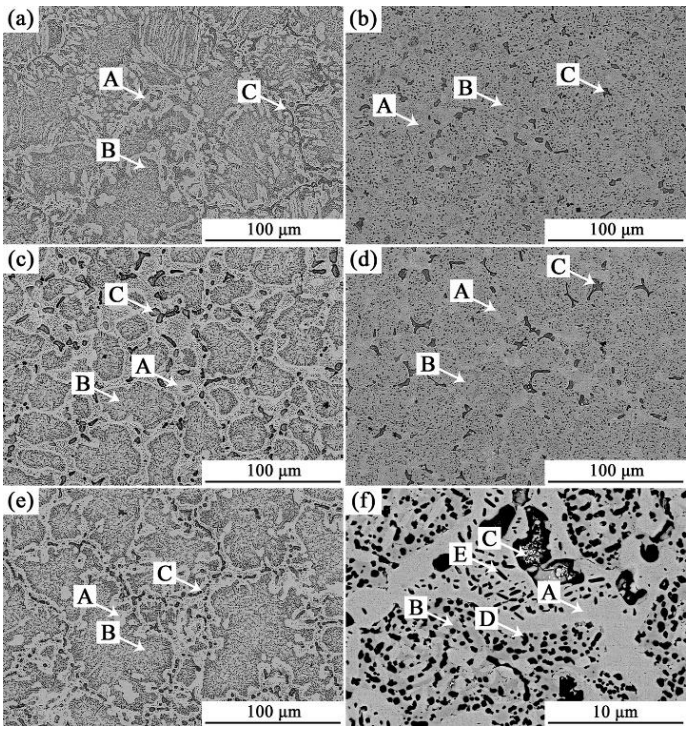

Figure 6. SEM-BSE image of the alloy after annealing: (a) A9T3; (b) A8T4; (c) A6T6; (d) A4T8; (e) A3T9; (f) A6T6.

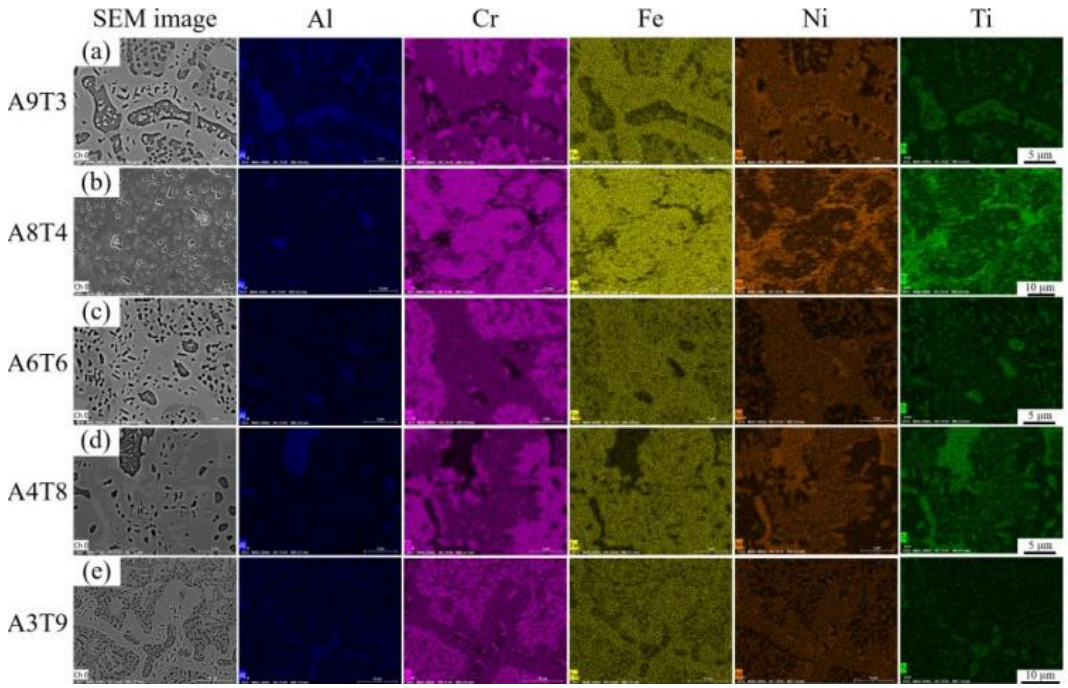

Figure 7. Surface scan of alloy after annealing: (a) A9T3; (b) A8T4; (c) A6T6; (d) A4T8; (e) A3T9.

Due to the similar microstructure of A9T3, A6T6, and A3T9 alloys pre and post annealing treatment, A6T6 alloy after annealing was selected as the target of study. Transmission electron microscopy was used to analyze the morphology and structure of dendrites and interdendritic structures of the alloy at the nanoscale. Figure 8a shows the bright -field TEM image of annealed A6T6 alloy, Figure 8c shows the bright-field image of precipitates in the dendritic structure, Figure 8b,d show the diffraction patterns along the [111] crystal band axis in the A and C regions of Figure 8c, Figure 8f shows a high-resolution TEM image of the interface area between the precipitate phase and the dendrite phase, Figure 8e,g show the diffraction patterns along the [111] crystal band axis in

 doi:10.20944/preprints202409.1787.v

the D and F regions of Figure 8f. As the figure shown, a large number of precipitation particles enriched with Ni, Ti, and Al elements are distributed on the dendritic structure, the size distribution ranges from a few hundred nanometers to a few micrometers. Based on the analysis results of high-resolution transmission (HRTEM) and SAED, the C and F regions correspond to diffraction patterns along the axis of the BCC phase [111] crystal belt, the interplanar spacing of crystal face (110) is approximately 0.204 nm. The A and D regions correspond to diffraction patterns along the axis of the B2 phase [111] crystal belt, the interplanar spacing of crystal face (110) is approximately 0.207 nm. Compared with the standard PDF card diffraction peak of the (110) crystal plane in Figure 1b, it can be determined that the phases in the C and F regions are BCC structured solid solution phases rich in [Fe, Cr], the D and F regions are B2 phases rich in Ni, Ti, and Al elements.

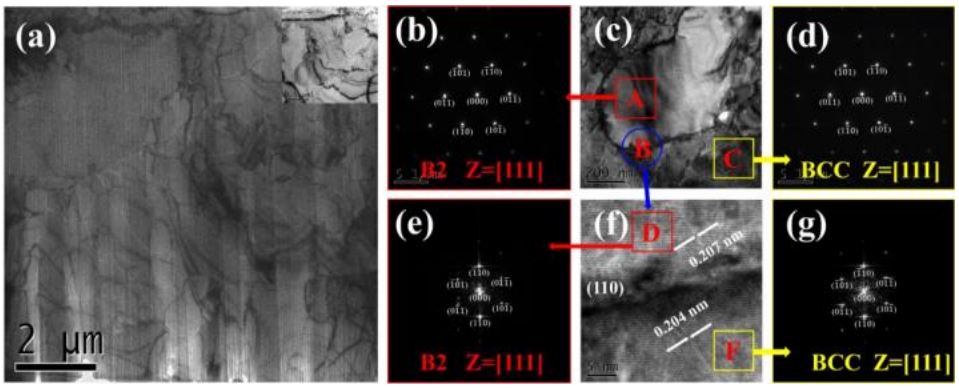

Figure 8. TEM images of annealed A6T6 alloy: (a) and (c) Bright-field images of annealed A6T6 alloy; (b) and (d) the corresponding SAED patterns of zone A and zone B along the [111] zone axis; (e) and (g) the corresponding SAED patterns of zone D and zone F along the [111] zone axis; (f) HRTEM of zone B.

Figure 9 shows the TEM image of the interdendritic structure of A6T6 alloy after annealing, Figure 9b shows the diffraction patterns along the [011] crystal band axis in region A of Figure 9a, Figure 9c shows the high-resolution TEM image of region A in Figure 9a, Figure 9d,e show the diffraction patterns along the [011] crystal band axis in the B and C regions of Figure 9c. Figure 9b shows the diffraction patterns along the axis of the [011] crystal band, weak superlattice diffraction spots can be observed. Figure 9c shows the high-resolution TEM image of region A in Figure 9a, we can observe the area of the triangle in lower right corner of Figure 9c, diffraction analysis was conducted on both sides of the area. Figure 9d shows the diffraction patterns along the [011] crystal band axis in the B region of Figure 9c, no presence of superlattice diffraction spots observed, the interplanar spacing of crystal face (111) is approximately 0.211 nm. Figure 9e shows the diffraction patterns along the [011] crystal band axis in the C region of Figure 9c, superlattice diffraction spots can be clearly observed, the interplanar spacing of crystal face (111) is approximately 0.212 nm. Compared with the standard PDF card diffraction peak of the (110) crystal plane in Figure 1b, we can determine that the corresponding phase in region B is FCC phase, the corresponding phase in region B is FCC phase, the phase in region C is $L1_2$ structured solid solution phase, the FCC phase maintains a good interfacial coherence with the $L1_2$ structured solid solution phase.

 doi:10.20944/preprints202409.1787.v

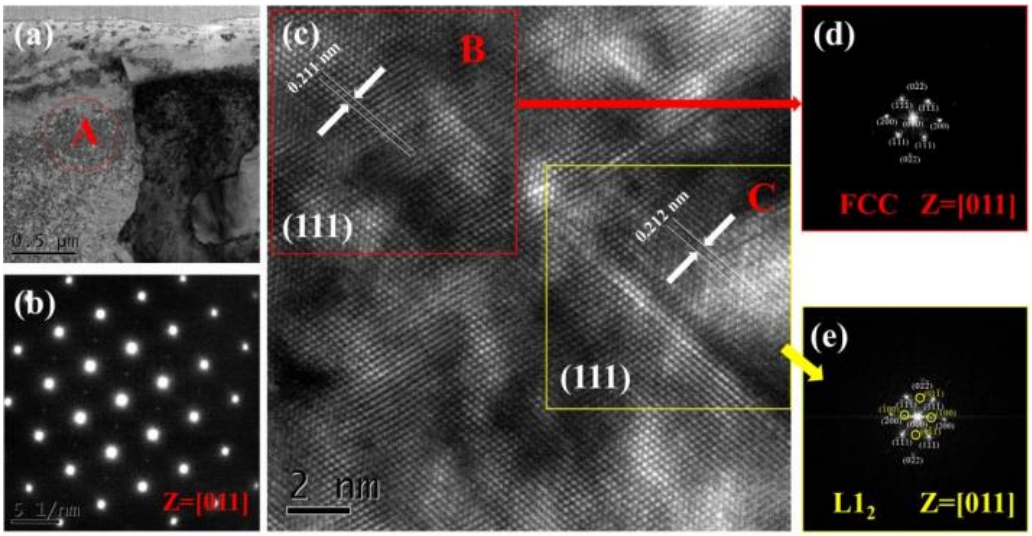

Figure 9. TEM images of annealed A6T6 alloy: (a) TEM images of dendrites; (b) the corresponding SAED patterns of zone A along the [011] zone axis; (c) HRTEM of zone A; (d) and (e) the corresponding SAED patterns of zone A and zone B along the [011] zone axis.

3.2. Analysis of Compressive Properties at Room Temperature

Figure 10 shows the engineering stress-strain curve of the sample, with a test strain rate of 2×10^{-4} s^{-1}. Table 5 illustrates the compressive property test results of as-cast alloys, including yield strength (σ0.2), fracture strength (σb), and deformation rate (εp). The data in Table 5 reveal that the σ0.2 of A8T4 alloy is lower than that of A9T3 alloy, decreasing from 1435.93 MPa to 1338.13 MPa, the fracture strength decreases from 2934.41 MPa to 2093.71 MPa, and the plastic strain decreases from 45.11% to 37.68%. The σ0.2 of the A6T6 sample is the highest, reaching 1707.41 MPa, and its σb and plastic strain are 3010.29 MPa and 41.05%. As the Ti content growth, the plastic strain of alloys continues to decrease. In comparison to the A9T3 alloy, the A3T9 alloy has better strength but poorer plasticity, with the lowest plastic strain at 18.71%.

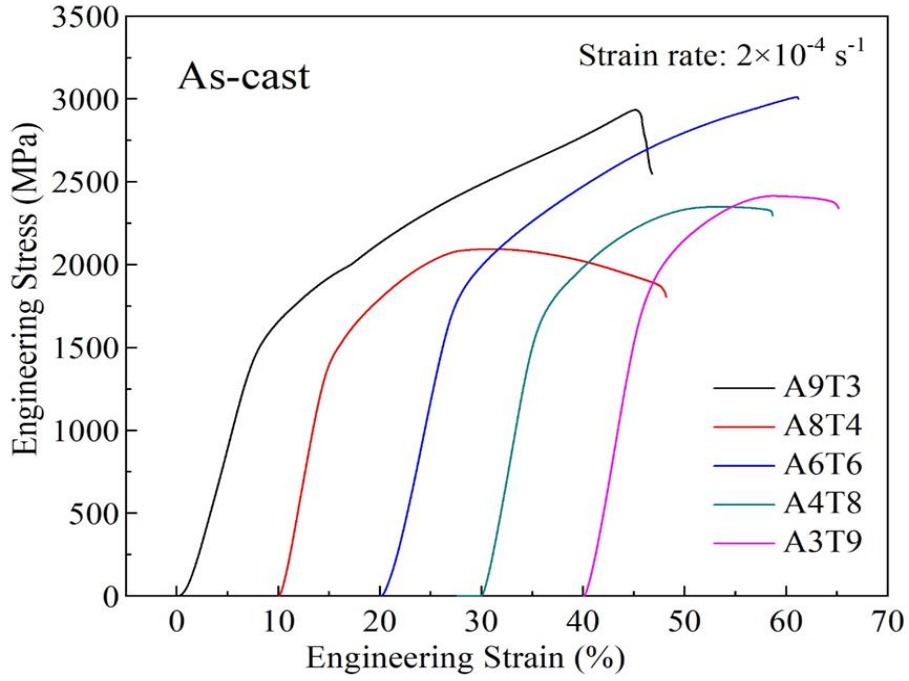

Figure 10. Compressive engineering stress-strain curves of as-cast alloys at room temperature.

 doi:10.20944/preprints202409.1787.v

Table 5. Compressive properties of as-cast $Al_x(CrFeNi)_{88}Ti_{(12-x)}$ alloys at room temperature.

alloy	$\sigma_{0.2}$(MPa)	σ_b(MPa)	ε_p(%)
$Al_9(CrFeNi)_{88}Ti_3$	1435.93	2934.41	45.11
$Al_8(CrFeNi)_{88}Ti_4$	1338.13	2093.71	37.68
$Al_6(CrFeNi)_{88}Ti_6$	1707.41	3010.29	41.05
$Al_4(CrFeNi)_{88}Ti_8$	1574.33	2348.89	26.12
$Al_3(CrFeNi)_{88}Ti_9$	1698.07	2413.99	18.71

The fracture morphology of cast alloy was observed after compressive mechanical properties testing using scanning electron microscopy in secondary electron mode, analyzing the fracture mechanism of alloy specimens. Figure 11 shows the microscopic morphology of the fracture surface of the as-cast alloy sample, A9T3 alloy has good plasticity, after compression testing, the sample did not break, bonded together. Therefore, the fracture surfaces of other samples were analyzed. Obvious dimple morphology was observed in Figure 11a,b, there are many concave or convex micro pits at the fracture surface, the second phase particles can be observed in the micro pits. In addition, flat and shiny dissociation fracture morphology was also observed, and many tearing edges, dissociation fracture mixed with dimples, belonging to typical quasi dissociation fracture. The morphology of dimples is less and the dissociation morphology is more in Figure 11c. In Figure 11d, the dissociation morphology is mainly observed, fewer dimples and more tearing edges can be observed, the dissociated layer structure can be watched, the overall morphology is mainly composed of small layers. A3T9 alloy still exhibits quasi dissociation fracture, but showing the greatest tendency towards brittleness. From Figure 11a–d, we can observe that as the Ti content growth, the plasticity of alloys gradually deteriorates, the fracture behavior of the alloy transfers from ductile fracture to brittle fracture.

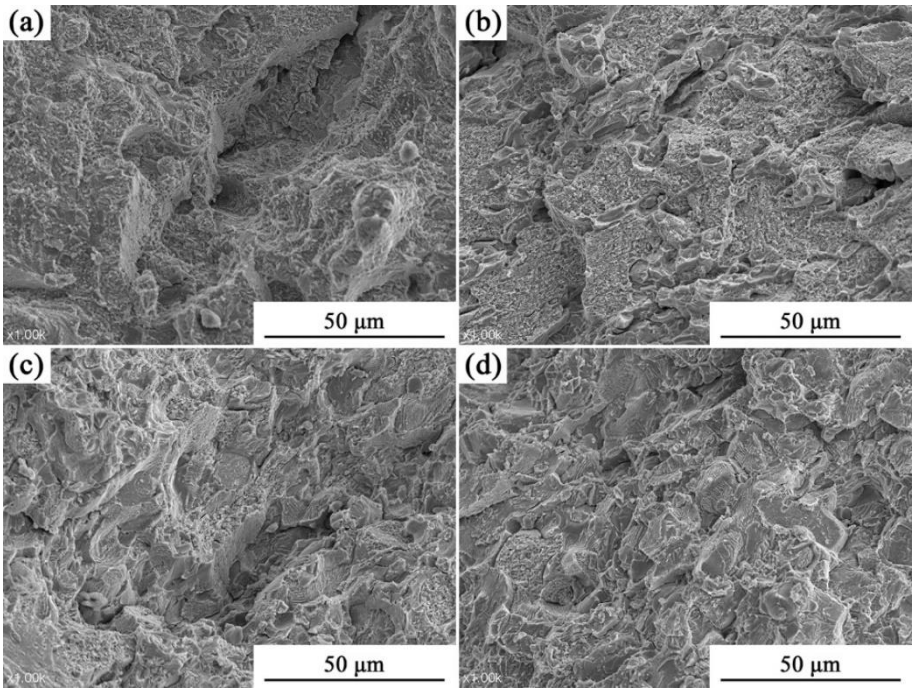

Figure 11. Compressive fracture morphology of as-cast Alx(CrFeNi)88Ti(12-x) alloy at room temperature: (a) A8T4; (b) A6T6; (c) A4T8; (d) A3T9.

Figure 12a illustrates the stress-strain curve of the compressive test of alloys after homogenization annealing heat treatment, with a test strain rate of 2×10^{-4} s^{-1}. Table 6 illustrates the compressive property test results of annealed alloys, including yield strength (σ0.2), fracture strength

 doi:10.20944/preprints202409.1787.v

(σb), and deformation rate (εp). Figure 12a reveals that the alloys after annealing have higher fracture strength (>2200MPa), while the plastic strain decreases to varying degrees. However, the change in yield strength is not regular due to the complex microstructure and morphology changes in the alloy after annealing heat treatment. After annealing, the uniform strength and fracture strength of A9T3 and A6T6 alloys decrease to different extents due to the reduction in the solid solution strengthening influence of Ti elements following homogenization of the composition. This is reflected in the decrease in hardness of the alloy after annealing. The relatively high yield strength of A6T6 alloy is owe to the smaller grain size and the increased presence of Ti atoms in solid solution. The microstructure of A8T4 and A4T8 alloys undergoes significant changes after annealing, presenting a high number of σ phases and a substantial increase in yield strength from the Ni_3Ti phase. A8T4 sample has the highest σ0.2 (2361.22 MPa) and σb (2602.28 MPa), with a low fracture strain is only 9.17%. After annealing, the σ0.2 of A3T9 sample increases, but the fracture strength decreases, leading to a lower plastic strain of 14.24%.

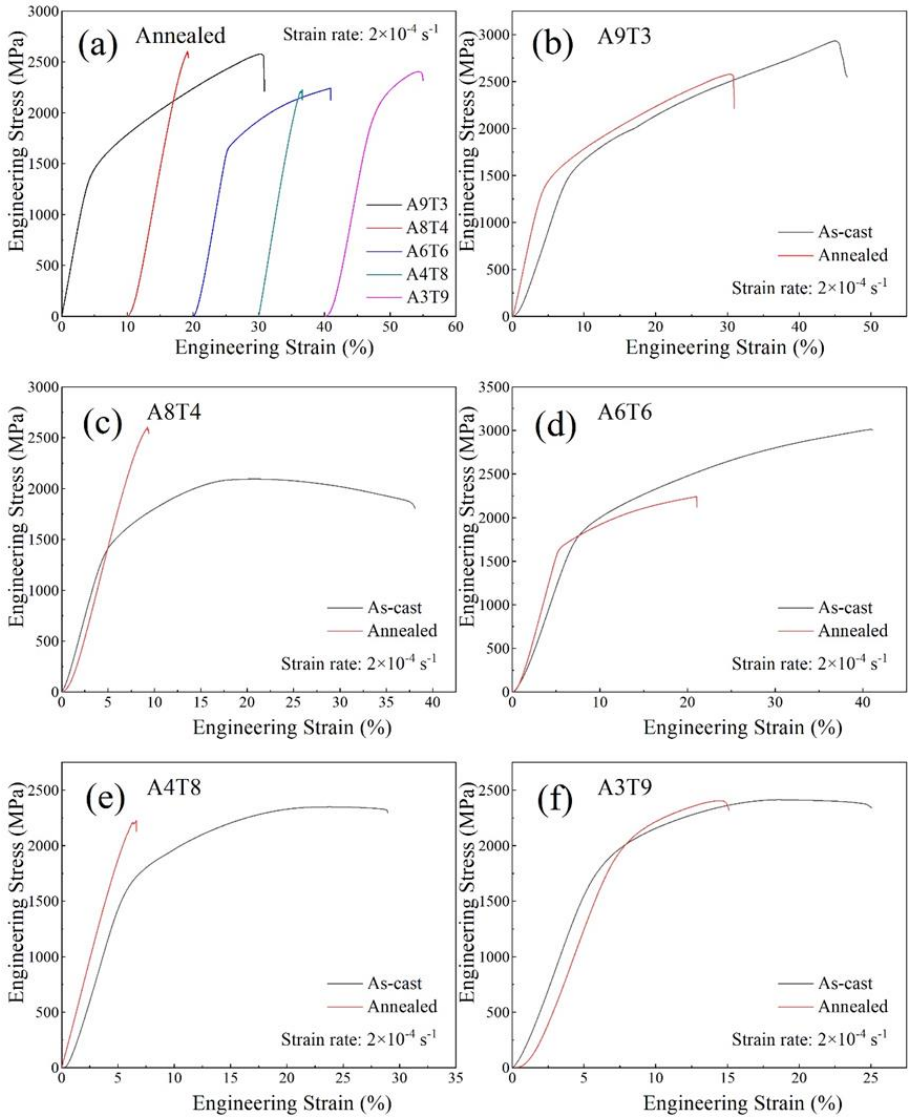

Figure 12. Compressive engineering stress-strain curves of alloys after annealing at room temperature (a); (b-f) comparison between as-cast and annealed states.

Table 6. Compressive properties of annealed $Al_x(CrFeNi)_{88}Ti_{(12-x)}$ alloys at room temperature.

alloy	$\sigma_{0.2}$(MPa)	σ_b(MPa)	ε_p(%)
$Al_9(CrFeNi)_{88}Ti_3$	1302.66	2578.01	30.22

 doi:10.20944/preprints202409.1787.v

$Al_8(CrFeNi)_{88}Ti_4$	2361.22	2602.28	9.17
$Al_6(CrFeNi)_{88}Ti_6$	1655.13	2242.45	20.94
$Al_4(CrFeNi)_{88}Ti_8$	1965.41	2227.09	6.63
$Al_3(CrFeNi)_{88}Ti_9$	1917.49	2404.25	14.24

Figure 13 reveals the fracture morphology of samples after room temperature compression mechanical properties testing of the annealed alloy, after prolonged annealing treatment, the plasticity of the alloy is significantly reduced. Obvious dimple morphology observed in Figure 13a,c, the second phase particles can be observed in the dimples, the particle size is coarser than that of cast alloys. The flat and shiny dissociation fracture morphology can also be observed, no friction marks observed on the surface of the fracture, dissociation fracture mixed with dimples, belonging to quasi dissociation fracture. There are compound precipitation in Figure 13b, which increase the brittleness of grain boundaries. There are obvious secondary cracks present, the secondary crack disperses the stress borne by the main crack during the deformation process of the after prolonged annealing treatment, the plasticity of the alloy is significantly reduced. Obvious dimple morphology observed in Figure 13a,c, the second phase particles can be observed in the dimples, the particle size is coarser than that of cast alloys. The flat and shiny dissociation fracture morphology can also be observed, no friction marks observed on the surface of the fracture, dissociation fracture mixed with dimples, belonging to quasi dissociation fracture. There are compound precipitation in Figure 13b, which increase the brittleness of grain boundaries. There are obvious secondary cracks present, the secondary crack disperses the stress borne by the main crack during the deformation process of the alloy, causes the alloy to exhibit high yield strength. The friction marks on the fracture surface after shear fracture can be seen in Figure 13b,d, the surface is very flat, presenting a river like pattern, it is the result of dissociating the step connection. There are also obvious secondary cracks in Figure 13d, indicates that A4T8 alloy has relatively high strength, belonging to dissociation fracture. Figure 13e shows a typical shear fracture morphology, which is caused by shear failure, friction marks appeared on the fracture surface, presenting a layered organizational morphology, belonging to quasi dissociation fracture. Compared to as-cast alloys, the plasticity of the alloy significantly decreases after annealing, the microstructure and morphology of A8T4 and A4T8 alloys have undergone significant changes, failure to maintain fracture behavior in the as-cast state.

 doi:10.20944/preprints202409.1787.v

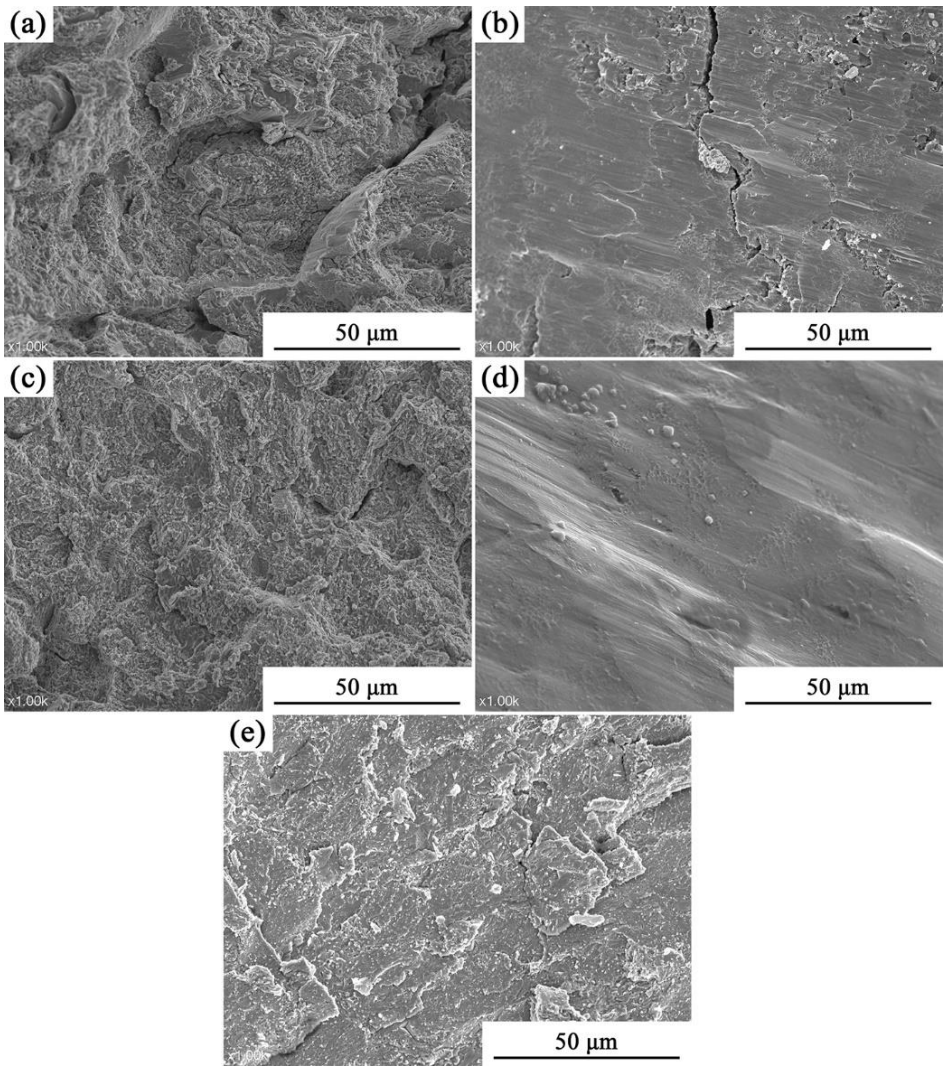

Figure 13. Compressive fracture morphology of annealed Alx(CrFeNi)88Ti(12-x) alloy at room temperature: (a) A9T3; (b) A8T4; (c) A6T6; (d) A4T8; (e) A3T9.

4. Conclusions

1) The as-cast $Al_x(CrFeNi)_{88}Ti_{(12-x)}$ alloy is primarily composed of BCC, FCC , B2 , and $L2_1$ phase and exhibits a typical dendrite structure, which remains unchanged even after prolonged annealing.
2) When the volume fraction of FCC phase in the cast alloy is high, the alloy tends to form σ Phase+Ni_3Ti phase after annealing. When the volume fraction of FCC phase is low, it will desolve and precipitate in a more stable L12 phase.
3) The addition of Ti to the as-cast alloy improves its strength and reduceds its plasticity, leading to a multiplication in yield strength from 1338.13 MPa to 1707.41 MPa and a decrease in plasticity from 45.11% to 18.71%. However, after annealing, the compressive properties of the alloy deteriorate, with only the yield strength increasing while both the fracture strength and plasticity decrease.

Author Contributions: Keyan An: Writing – original draft, Formal analysis, Validation, Investigation, Methodology. **Tailin Yang:** Validation, Formal analysis. **Junjie Feng:** Validation. **Honglian Deng**: Validation. **Zhang Xiang**: Validation. **Zeyu Zhao**: Validation. **Qingkun Meng**: Validation. **Jiqiu Qi**: Validation. **Fuxiang Wei:** Validation. **Yanwei Sui:** Writing - Review & Editing, Supervision, Funding acquisition.

Data Availability: The data that support the findings of this study are available from corresponding author upon reasonable request.

Acknowledgments: This work was financially supported by the National Natural Science Foundation of China (52171227) and Xuzhou Science and Technology Project (kc22483).

 doi:10.20944/preprints202409.1787.v

Conflicts of Interest: The authors declare that they have no known competing financial interests or personal relationships that could have appeared to influence the work reported in this paper.

References

1. Joseph J, Senadefra M, Chao Q, et al. Computational design of thermally stable and precipitation-hardened Al-Co-Cr-Fe-Ni-Ti high entropy alloys, Journal of Alloys and Compounds, 2021, 888 161496.
2. Kim m J, Kang G C, Hong S H, Park H J, Mun S C, Song G, Kim K B. Understanding microstructure and mechanical properties of $(AlTa_{0.76})_xCoCrFeNi_{2.1}$ eutectic high entropy alloys via thermo-physical parameters, Journal of Materials Science & Technology, 2020, 57 131−137.
3. Makhmutov T, Razumov N, Kim A, et al. Synthesis of $CoCrFeNiMnW_{0.25}$ High-Entropy Alloy Powders by Mechanical Alloying and Plasma Spheroidization Processes for Additive Manufacturing, Metals and Materials International, 2021, 27(1) 50-54.
4. Yang Cheng-bo, Zhang Jing, Li Meng, Liu Xue-jian. Soft-magnetic high-entropy AlCoFeMnNi alloys with dual-phase microstructures induced by annealing, Acta Metallurgica Sinica (English Letters), 2020, 33(8) 1124−1134.
5. Zhang Y P, Shen Q K, Chen X Z, et al. Strengthening Mechanisms in $CoCrFeNiX_{0.4}$ (Al, Nb, Ta) High Entropy Alloys Fabricated by Powder Plasma Arc Additive Manufacturing, Nanomaterials, 2021, 11(3) 721.
6. Peng Jian, Li Zi-yong, Ji Xin-bo, Sun Yan-le, Fu Li-ming, Shan Ai-dang. Decomposition kinetics of carbon-doped FeCoCrNiMn high-entropy alloy at intermediate temperature, Transactions of Nonferrous Metals Society of China, 2020, 30(7) 1884−1894.
7. Jiang H, Qiao D X, Jiao W N, et al. Tensile deformation behavior and mechanical properties of a bulk cast $Al_{0.9}CoFeNi_2$ eutectic high-entropy alloy, Journal of Materials Science & Technology, 2021, 61 119-124.
8. Jiang Hui, Qiao Dong-xu, Jiao Wen-na, Han Kai-ming, Lu Yi-ping, Liaw P K. Tensile deformation behavior and mechanical properties of a bulk cast $Al_{0.9}CoFeNi_2$ eutectic high-entropy alloy, Journal of Materials Science & Technology, 2021, 61 119−124.
9. Y. Yuan, J.J. Wang, J. Wei, W.Y. Chen, H.L. Yan, N. Jia, Cu alloying enables superior strength-ductility combination and high corrosion resistance of FeMnCoCr high entropy alloy, Journal of Alloys and Compounds,970, 2024, 172543.
10. Zhen Zhang, Xiaofeng Li, Hong Yi, Huiqi Xie, Zhanyong Zhao, Peikang Bai, Clarify the role of Nb alloying on passive film and corrosion behavior of CoCrFeMnNi high entropy alloy fabricated by laser powder bed fusion, Corrosion Science, 224, 2023, 111510.
11. Binbin Liu, Jia Li, Martin Peterlechner, Heng Zhang, Yuan Wu, Gerhard Wilde, Feng Ye, Microstructure and mechanical properties of Si micro-alloyed $(Ti_{28}Zr_{40}Al_{20}Nb_{12})_{100-x}Si_x$ $(x=0,\ 0.1,\ 0.2,\ 0.5)$ high entropy alloys, Intermetallics, 161, 2023, 107959.
12. Gao Shuo, Kong Teng, Zhang Man, Chen Xiao, Sui Yan-wei, Ren Yao-jian, Qi Ji-qiu, WeI Fu-xiang, He Ye-zeng, Meng Qing-kun, Sun Zhi. Effects of titanium addition on microstructure and mechanical properties of $CrFeNiTi_x$ (x=0.2−0.6) compositionally complex alloys, Journal of Materials Research, 2019, 34(5) 819−828.
13. Wang L L, Zhou J Q, Liu H X, et al. Severe grain rotation behavior of $L1_2$-B2 nano lamellar eutectic structure, Materials Letters, 2021, 302: 130393.
14. Cao Yuan-kui, Liu Yong, Liu Bin, Zhang Wei-dong, Wang Jia-wen, Du Meng. Effects of Al and Mo on high temperature oxidation behavior of refractory high entropy alloys, Transactions of Nonferrous Metals Society of China, 2019, 29(7) 1476−1483.
15. Guo R, Pan J, Liu L. Achieving dual-phase structure and improved mechanical properties in $AlCoCrFeTi_{0.5}$ high-entropy alloys by addition of Ni, Materials Science and Engineering: A, 2022, 831 142194.
16. Abhishek M, Yong H S. Fundamental Core Effects in Transition Metal High-Entropy Alloys: “High-Entropy” and “Sluggish Diffusion” Effects, Diffusion Foundations, 2021, 29 75-93.
17. Cai YC, Zhu LS, Cui Y, et al. Influence of high-temperature condition on the microstructure and properties of $FeCoCrNiAl_{0.3}$ and $FeCoCrNiAl_{0.7}$ high-entropy alloy coatings, Surface Engineering, 2021, 37(2) 179-187.
18. Gong X, Xiang C Y, Auger T, et al. Liquid metal embrittlement of a dual-phase $Al_{0.7}CoCrFeNi$ high-entropy alloy exposed to oxygen-saturated lead-bismuth eutectic, Scripta Materialia, 2021, 194 113652.
19. Wen X, Cui X F, Jin G, et al. In-situ synthesis of nano-lamellar $Ni_{1.5}CrCoFe_{0.5}Mo_{0.1}Nb_x$ eutectic high-entropy alloy coatings by laser cladding: Alloy design and microstructure evolution, Surface & Coatings Technology, 2021, 405 126728.
20. Feng S, Fu H D, Zhou H Y, et al. A general and transferable deep learning framework for predicting phase formation in materials, npj Computational Materials, 2021, 7(1) 1-10.
21. Yan Y R, Fang L Y, Tan Y K, Tao X M, Ouyang Y F, Du Y. Mechanical properties and corrosion resistance of $Al_xCoCuFeMn$ high-entropy alloys, Journal of Materials Research and Technology, 2023, 24 5250-5259.
22. Zhang M D, Ma Y M, Dong W Q, et al. Phase evolution, microstructure, and mechanical behaviors of the $CrFeNiAl_xTi_y$ medium-entropy alloys, Materials Science and Engineering: A, 2020, 771 138566.

 doi:10.20944/preprints202409.1787.v

23. Kao W H, Su Y L, Horng J H, et al. Mechanical, tribological, anti-corrosion and anti-glass sticking properties of high-entropy TaNbSiZrCr carbide coatings prepared using radio-frequency magnetron sputtering, Materials Chemistry and Physics, 2021, 268 124741.
24. Li Y T, Wang C T, Ma D L, et al. Nano dual-phase CuNiTiNbCr high entropy alloy films produced by high-power pulsed magnetron sputtering, Surface & Coatings Technology, 2021, 420 127325.
25. Kumar A, Singh A, Suhane A. A critical review on mechanically alloyed high entropy alloys: processing challenges and properties, Materials Research Express, 2022, 9(5): 52001.
26. Zhang G Z, Liu H, Tian X H, et al. Microstructure and Properties of AlCoCrFeNiSi High-Entropy Alloy Coating on AISI 304 Stainless Steel by Laser Cladding, Journal of Materials Engineering and Performance, 2020, 29(1) 278-288.
27. Qiu H, Zhu H G, Zhang J F, et al. Effect of Fe content upon the microstructures and mechanical properties of $Fe_xCoNiCu$ high entropy alloys, Materials Science & Engineering: A, 2020, 769 138514.
28. Wang H J, Wu Z Y, Wu H, et al. In Situ TiC Particle-Reinforced FeCoCrNiCu High Entropy Alloy Matrix Composites by Induction Smelting, Transactions of the Indian Institute of Metals, 2021, 74(2) 267-272.
29. Jin B Q, Zhang N N, Zhang Y, et al. Microstructure, phase composition and wear resistance of low valence electron concentration $Al_xCoCrFeNiSi$ high-entropy alloys prepared by vacuum arc melting, Journal of Iron and Steel Research International, 2020, 28(2) 181- 189.
30. Suprianto, Chen C L. Study of (Ni, Cr) pre-milling for synthesis of CoFe(NiCr)Mn high entropy alloy by mechanical alloying, Materials Science & Engineering: A, 2021, 807 140810.
31. Hansol S, Seungjin N, Hyunjoo C. Development of porous high-entropy alloys by mechanical alloying and chemical de-alloying, Powder Metallurgy, 2021, 64(3) 211-218.
32. Wu X X, Mayweg D, Ponge D, et al. Microstructure and deformation behavior of two TWIP/TRIP high entropy alloys upon grain refinement, Materials Science & Engineering: A, 2021, 802 140661.
33. Marianac, Jithin V, Pramote T, et al. Tailoring biocompatible Ti-Zr-Nb-Hf-Si metallic glasses based on high-entropy alloys design approach, Materials science & engineering C, Materials for biological applications, 2021, 121: 111733.
34. Miklós K D, Nikolett M P, Éva F. Examination of microstructure and corrosion properties of novel AlCoCrFeNi multicomponent alloy, Materials Today: Proceedings, 2021, 45(5) 4250- 4253.